Bioactive Materials 34 (2024) 51–63

Contents lists available at ScienceDirect

Bioactive Materials

journal homepage: www.keaipublishing.com/en/journals/bioactive-materials

Adipose-derived mesenchymal stem cells (MSCs) are a superior cell source for bone tissue engineering

Yannian Gou [a,b], Yanran Huang [a,c], Wenping Luo [d], Yanan Li [e], Piao Zhao [a,b,c], Jiamin Zhong [a,b], Xiangyu Dong [a], Meichun Guo [a], Aohua Li [a], Ailing Hao [a], Guozhi Zhao [b,c], Yonghui Wang [b,f], Yi Zhu [b,g], Hui Zhang [b,h], Yunhan Shi [b,i,j], William Wagstaff [b], Hue H. Luu [b], Lewis L. Shi [b], Russell R. Reid [b,k], Tong-Chuan He [b,k,*], Jiaming Fan [a,**]

[a] *Ministry of Education Key Laboratory of Diagnostic Medicine, and Department of Clinical Biochemistry, School of Laboratory Medicine, Chongqing Medical University, Chongqing, 400016, China*
[b] *Molecular Oncology Laboratory, Department of Orthopaedic Surgery and Rehabilitation Medicine, The University of Chicago Medical Center, Chicago, IL, 60637, USA*
[c] *Departments of Orthopedic Surgery and Urology, The First Affiliated Hospital of Chongqing Medical University, Chongqing, 400016, China*
[d] *Laboratory Animal Center, Southwest University, Chongqing, 400715, China*
[e] *Chongqing Key Laboratory of Oral Diseases and Biomedical Sciences, The Stomatological Hospital of Chongqing Medical University, Chongqing, 401147, China*
[f] *Department of Geriatrics, Xinhua Hospital, Shanghai Jiao-Tong University School of Medicine, Shanghai, 200000, China*
[g] *Department of Orthopaedic Surgery, Beijing Hospital, Chinese Academy of Medical Sciences & Peking Union Medical College, Beijing, 100730, China*
[h] *The Breast Cancer Center, Chongqing University Cancer Hospital, Chongqing, 4000430, China*
[i] *Department of Psychology, School of Arts and Sciences, University of Rochester, Rochester, NY, 14627, USA*
[j] *Department of Surgery, The University of Chicago Medical Center, Chicago, IL, 60637, USA*
[k] *Laboratory of Craniofacial Biology and Development, Department of Surgery Section of Plastic Surgery, The University of Chicago Medical Center, Chicago, IL, 60637, USA*

ARTICLE INFO

Keywords:
Mesenchymal stem cell (MSC)
Bone tissue engineering
Multipotent progenitor cells
Adipose-derived mesenchymal stem cells
Osteogenic differentiation
Adipogenesis

ABSTRACT

Effective bone regeneration through tissue engineering requires a combination of osteogenic progenitors, osteoinductive biofactors and biocompatible scaffold materials. Mesenchymal stem cells (MSCs) represent the most promising seed cells for bone tissue engineering. As multipotent stem cells that can self-renew and differentiate into multiple lineages including bone and fat, MSCs can be isolated from numerous tissues and exhibit varied differentiation potential. To identify an optimal progenitor cell source for bone tissue engineering, we analyzed the proliferative activity and osteogenic potential of four commonly-used mouse MSC sources, including immortalized mouse embryonic fibroblasts (iMEF), immortalized mouse bone marrow stromal stem cells (imBMSC), immortalized mouse calvarial mesenchymal progenitors (iCAL), and immortalized mouse adipose-derived mesenchymal stem cells (iMAD). We found that iMAD exhibited highest osteogenic and adipogenic capabilities upon BMP9 stimulation *in vitro*, whereas iMAD and iCAL exhibited highest osteogenic capability in BMP9-induced ectopic osteogenesis and critical-sized calvarial defect repair. Transcriptomic analysis revealed that, while each MSC line regulated a distinct set of target genes upon BMP9 stimulation, all MSC lines underwent osteogenic differentiation by regulating osteogenesis-related signaling including Wnt, TGF-β, PI3K/AKT, MAPK, Hippo and JAK-STAT pathways. Collectively, our results demonstrate that adipose-derived MSCs represent optimal progenitor sources for cell-based bone tissue engineering.

Peer review under responsibility of KeAi Communications Co., Ltd.

* Corresponding author. Molecular Oncology Laboratory, Department of Orthopaedic Surgery and Rehabilitation Medicine, The University of Chicago Medical Center, Chicago, IL, 60637, USA.
** Corresponding author.
E-mail addresses: urbanekou@foxmail.com (Y. Gou), yanran-huang@boneandcancer.org (Y. Huang), lwplucky@163.com (W. Luo), yanan-li@boneandcancer.org (Y. Li), cecilialanmon@qq.com (P. Zhao), 1564094338@qq.com (J. Zhong), xydong2151@163.com (X. Dong), 1274664809@qq.com (M. Guo), 18364057370@163.com (A. Li), 2996870689@qq.com (A. Hao), 494475057@qq.com (G. Zhao), wangzimian1100@163.com (Y. Wang), sdzhuyi@foxmail.com (Y. Zhu), huizhang0703@foxmail.com (H. Zhang), yshi29@u.rochester.edu (Y. Shi), wagstaff@uchicago.edu (W. Wagstaff), hluu@bsd.uchicago.edu (H.H. Luu), lshi@bsd.uchicago.edu (L.L. Shi), rreid@bsd.uchicago.edu (R.R. Reid), tche@uchicago.edu (T.-C. He), fanjiaming1988@cqmu.edu.cn (J. Fan).

https://doi.org/10.1016/j.bioactmat.2023.12.003
Received 19 September 2023; Received in revised form 26 November 2023; Accepted 2 December 2023

1. Introduction

As an essential part of the locomotor system, bone plays important roles in bone marrow generation, calcium and phosphorus storage, and protection of internal organs [1,2]. While being one of a few organs in our body that maintain regenerative ability throughout lifetime, bone can suffer from large defects that are beyond the intrinsic regenerative capacity, such as traumatic injuries, fractures, and surgical resection of tumors. Since the delayed or poor bone defect healing has serious negative impact on the quality of life and/or survival of the affected individuals, it is usually necessary to use bone grafts to accelerate the healing of damaged bone [2–4]. However, persistent pain, long recovery time, risks of infection and resorption, and other donor site morbidities limit the potential applications of autogenous and allogenous grafts bone [2–4]. Bone tissue engineering approaches have emerged as a promising alternative to overcome the limitations of bone grafts [2–4].

Successful bone tissue engineering requires a combination of multipotent stem/progenitor cells [5–8], growth/osteogenic factors [9–16], and biocompatible scaffold materials [17], in which osteogenic progenitors represent an important component of any efficacious bone tissue engineering strategy. Through a comprehensive analysis of 14 types of human bone morphogenetic proteins (BMPs), we previously identified the BMP9 as the most potent osteogenic factor to induce osteogenic differentiation *in vitro* and *in vivo* [11,18–20]. While numerous studies have reported that embryonic stem cells (ESCs) [21] and induced pluripotent stem cells (iPSCs) [22] have the characteristics of proliferative and osteogenic differentiation capabilities, adult stem cells, mostly mesenchymal stem cells (MSCs) are the most promising seed cells for bone tissue engineering due to their abundance and easy accessibility [5–8,23]. MSCs are multipotent stem cells that can undergo self-renewal and differentiate into multiple cell lineages such as bone, cartilage, fat and muscle [5–7,23]. Even though bone marrow stromal-derived stem cells (BMSCs) are considered prototypic MSCs, it is well known now that MSCs can be isolated from various tissues, most notably adipose tissue [5–7,23]. However, the osteogenic and bone defect repair profiles of the different MSC sources have yet to be compared.

In order to identify an optimal progenitor source for bone tissue engineering applications, we conducted a comprehensive comparative analysis of the proliferative activity and osteogenic potential of four commonly-used MSC sources, including immortalized mouse embryonic fibroblasts (iMEF) [24,25], immortalized mouse bone marrow stromal stem cells (imBMSC) [26], immortalized mouse calvarial mesenchymal progenitors (iCAL) [27], and immortalized mouse adipose-derived mesenchymal stem cells (iMAD) [28]. Given the fact that these MSC lines are reversibly immortalized and retain MSC multipotency with osteogenic, chondrogenic and adipogenic differentiation potential [24,29–34], the four MSC lines provide a unique platform for comparing the osteogenic capacity of MSCs derived from different tissues in a comprehensive fashion. Our results demonstrate that iMADs exhibited the strongest osteogenic and adipogenic capabilities upon BMP9 stimulation *in vitro*. *In vivo* studies employing ectopic osteogenesis and critical-sized calvarial defect repair model revealed that iMAD and iCAL cells exhibited the highest osteogenic capability. Transcriptomic analysis indicated that, while each MSC line regulated a distinct set of target genes, all four MSC lines underwent osteogenic differentiation by regulating several osteogenesis-related signaling pathways, including Wnt, TGF-β, PI3K/AKT, MAPK, Hippo and Jak-STAT signaling pathways. Collectively, our results demonstrate that adipose-derived MSCs represent one of the best progenitor sources for cell-based bone tissue engineering applications.

2. Materials and Methods

2.1. Cell culture and chemicals

The four types of mouse MSC lines, immortalized mouse embryonic fibroblasts (iMEF) [24,25], immortalized mouse adipose-derived mesenchymal stem cells (iMAD) [28], immortalized mouse calvarial mesenchymal progenitors (iCAL) [27], and immortalized mouse bone marrow stromal stem cells (imBMSC) [26] were previously characterized. Human HEK293-derived lines 293pTP and RAPA cells were also described previously [35,36], and used for recombinant adenovirus packaging and amplification. All cells were cultured in high glucose complete Dulbecco's modified Eagle's medium (DMEM) supplemented with 10 % FBS (LONSA SCIENCE SRL, Uruguay), 100 units of penicillin and 100 μg % of streptomycin at 37 °C in 5 % CO_2 as described [37–41].

For osteogenic induction, these cells were cultured in osteogenic medium (0.1 μM Dexamethasone, 50 μM vitamin C and 10 mM β-sodium glycerophosphate) for varied time periods as reported [18,41–43]. Unless indicated otherwise, all other chemicals were purchased from Sigma-Aldrich (St Louis, MO), Thermo Fisher Scientific (Pittsburgh, PA), or Solarbio (Beijing, China).

2.2. Crystal violet cell viability assay

Subconfluent cells were seeded in 24-well plates. At the indicated time points, the cells were gently washed with PBS and stained with 0.5 % crystal violet/formalin solution for 10 min. The stained cells were washed with tap water and air-dried for scanning. The staining images were recorded under a bright field microscope. For quantitative analysis, the stained cells were dissolved in 10 % acetic acid and measured for absorbance at 592 nm as described [44–47]. Each assay condition was done in triplicate.

2.3. WST-1 cell proliferation assay

Subconfluent cells were seeded in 96-well plates. At the indicated time points, the Premixed WST-1 Reagent (Clontech, Mountain View, CA) was added, incubated at 37 °C for 120 min, followed by reading absorbance at 450 nm using a microplate reader (Biotek, EON, USA) as described [48–51]. Each assay condition was performed in triplicate.

2.4. RNA isolation and touchdown-quantitative real-time PCR (TqPCR)

Total RNA was isolated by using the TRIZOL Reagent (Invitrogen, China), and subjected to reverse transcription using hexamer and M-MuLV reverse transcriptase (New England Biolabs, Ipswich, MA). The cDNA products were used as PCR templates. Gene-specific PCR primers were designed by using Primer3 program (Table S1). TqPCR was carried out by using 2x SYBR Green qPCR Master Mix (Bimake, Shanghai, China) on a CFX-Connect unit (Bio-Rad Laboratories, Hercules, CA) as described [52,53]. All TqPCR reactions were done in triplicate. *Gapdh* was used as a reference gene. Quantification of gene expression was carried out by using the $2^{-\Delta\Delta Cq}$ method as described [32,51,54–56]. Clustering heatmap analysis of relative gene expression was carried out by using the pheatmap package in R (4.2.2).

2.5. Immunofluorescence (IF) staining

The IF staining was carried out as previously described [25,37,57]. Briefly, cells were seeded and treated in chamber slides, fixed with 4 % paraformaldehyde for 15 min at RT, treated with 0.5 % Triton X-100 for 20 min, and blocked with 5 % goat serum (1:10 dilution) for 20 min at RT, followed by incubation with primary antibodies against CD105 (1:100 dilution; Proteintech; Cat# 10862-1-AP), NANOG (1:100 dilution; Proteintech; Cat# 14295-1-AP), ACTA2 (1:50 dilution; Bimake; Cat# A5550), HAND1 (1:100 dilution; Bioworld; Cat# MB63487) or PPARγ (1:100 dilution; Affinity; Cat# AF6284) overnight. After being washed, the cells were incubated with goat anti-rabbit IgG/APC (1:200 dilution; Bioss; Cat# bs-0295G-APC) or CoraLite594 – conjugated Goat Anti-Rabbit IgG (H + L) (1:200 dilution; Proteintech; Cat# SA00013-4) or Fluorescein (FITC)–conjugated Affinipure Goat Anti-Rabbit IgG(H +

L) (1:200 dilution; Proteintech; Cat No. SA00003-2). The cell nuclei were counterstained with DAPI (10 μg/mL). Minus primary antibodies were used as negative controls. IF staining results were recorded under a confocal microscope (Leica TCS SP8).

2.6. Construction and amplification of the recombinant adenoviruses Ad-B9, AdR-B9, Ad-GFP and Ad-RFP

All recombinant adenoviruses were constructed by using the AdEasy technology as described [58–60]. The Ad-B9 co-expresses human BMP9 and GFP, whereas AdR-B9 co-expresses mouse BMP9 and RFP as described in our previous studies [18–20]. An analogous adenovirus expressing GFP or RFP only, Ad-GFP or Ad-RFP, was used as a mock virus control [35,54,61–63].

2.7. Qualitative and quantitative assays of alkaline phosphatase (ALP) activity

Subconfluent cells were seeded in 24-well plates and treated with osteogenic medium (normal medium as the control), or infected with Ad-B9 (Ad-GFP as the control), respectively. ALP activity was qualitatively assessed with histochemical staining assay (BCIP/NBT Alkaline phosphatase color development Kit, beyotime, Cat# C3206), while ALP activity was quantitatively analyzed with the Native Lysis Buffer (Solarbio, Cat#R0030) and the AKP/ALP activity test kit (Solarbio, Cat#BC2145) at indicated time points as described [43,64,65]. The staining images were documented under a bright field microscope. Each assay condition was done in triplicate.

2.8. Alizarin red staining

The Alizarin red staining was carried out as previously reported [31,32,43]. Briefly, cells were seeded in 24-well plates, treated with osteogenic medium or normal medium, or infected with Ad-B9 or Ad-GFP, respectively. At the indicated time points, cells were fixed with 4 % paraformaldehyde at RT for 10 min and washed with distilled water. The fixed cells were incubated with 0.4 % Alizarin red S for 5 min, followed by extensive washing with distilled water. The stained calcium mineral deposits were documented under a bright field microscope. Each assay condition was done in triplicate.

2.9. Oil Red O staining

Cells were seeded in 24-well culture plates and treated with AdR-B9 or Ad-RFP. Alternatively, frozen sections from freshly retrieved subcutaneous implant masses in nude mice were washed with PBS to remove the embedding agents. The Oil red O staining was carried out as previously reported [19,54,66,67]. Specifically, both cultured cells and frozen sections were fixed with 4 % paraformaldehyde for 10 min, briefly incubated in 60 % isopropanol, and then stained with freshly-prepared Oil Red O solution for 5 min, followed by PBS washes. The staining results were recorded under a bright field microscope. Each assay condition was done in triplicate.

2.10. Bodipy 493/503 staining

Bodipy 493/503 fluorescent detection of lipid droplets was carried out as reported [54,68]. Cells were seeded in 24-well culture plates and infected with AdR-B9 or Ad-RFP. The cells were fixed with 4 % paraformaldehyde for 10 min, lipid droplets were stained with 30 μmol/L BODIPY493/503 (Sigma-Aldrich), and the nuclei were stained with DAPI for 5 min, followed by PBS washes. The results were recorded under a fluorescence microscope. Each assay condition was done in triplicate.

2.11. Subcutaneous ectopic bone formation in athymic nude mice

The use and care of experimental animals was approved by the Research Ethics and Regulations Committee of Chongqing Medical University, Chongqing, China. All experimental procedures followed the approved guidelines. Athymic nude mice were obtained from and housed in the Experimental Animal Research Center of Chongqing Medical University. Stem cell-based ectopic bone formation was performed as previously described [69–75]. Briefly, subconfluent cells were infected with Ad-B9 or Ad-GFP for 36 h, collected and resuspended in sterile PBS for subcutaneous injection into the flanks of athymic nude mice (5–6 week old, male, 5×10^6 cells/injection, 6 injections per mouse, and 3 mice per group). At 28 days after injection, mice were sacrificed, and subcutaneous masses at the injection sites were retrieved. No masses were detected in the Ad-GFP injection group.

2.12. Gelatin methacryloyl (GelMA) hydrogel-MSC cell mixture

GelMA hydrogel was synthesized and characterized as previously described [76]. The concentrations of GelMA, UV cross-linking duration, and numbers of MSC cells were optimized as shown in Fig. S9A, panel a & b. Briefly, 5 % or 10 % GelMA mixed with 10^5 or 10^6 iMEF cells in 30 μL PBS were seeded in 96-well plates, exposed to UV irradiated (UV 365 nm, 3.7 V, 15 W) for 30 s, 60 s and 120 s, respectively, followed by adding 200 μL complete DMEM medium for observing color changes of the medium after 48 h. WST-1 assay was carried out to assess cell proliferation.

For the calvarial defect repair model shown in Fig. S9B, panel a–c, 10^6 cells infected with Ad-GFP mixed with 5 % GelMA in 100 μL PBS, seeded in 96-well plates, treated with UV irradiation for 30 s, then added 200 μL complete DMEM medium, observed the color change of the medium at day 0, 1, 2, 3 and 4. WST-1 assay was carried out to assess cell proliferation.

2.13. Mouse model of critical-sized calvarial defect

Athymic nude mice were obtained from and housed in the Experimental Animal Research Center of Chongqing Medical University. The critical-sized mouse calvarial defect model was established as previously described [77–79]. Briefly, athymic nude mice (4–6 week old, male, 4 mice per group) were anesthetized by intraperitoneal injection of 3 % sodium pentobarbital at 50 mg/kg body weight. As shown in Fig. S9C, panel a–c, under sterile conditions, an incision was made on the vertex scalp, and the skin was pulled apart to the sides to expose the calvaria. A 4 mm-diameter calvarial defect was created on the left parietal bone of each mouse with a multifunctional micro electric stainless-steel drill. 30 μL of 5 % GelMA-MSC mixture (containing 10^6 of iMAD, iMEF, iCAL or imBMSC cells infected with Ad-B9 or Ad-GFP) was instilled into the defect, followed by 30 s of UV exposure to solidify the hydrogel-cell mix. The incision was closed with 4–0 nylon interrupted sutures. At 4 weeks after implantation, mice were sacrificed, and calvarial samples were retrieved and fixed for μCT imaging and histologic analysis.

2.14. Micro-computed tomographic (μCT) imaging analysis

The retrieved subcutaneous samples and calvarial specimens were fixed in 4 % paraformaldehyde, and imaged with the Bruker Micro-CT Skyscan 1276 system (Kontich, Belgium) as described [80–82]. The scanning parameters were as follows: voxel size 6.533712 μm, medium resolution, 85 kV, 200 μA, 1 mm Al filter, and integration time 384 ms. Density measurements were calibrated to the manufacturer's calcium hydroxyapatite (CaHA) phantom. Data analysis was performed using the manufacturer's evaluation software. Reconstruction was accomplished by NRecon (version 1.7.4.2). The 3-D images were obtained from contoured 2D images based on distance transformation of the grayscale original images (CTvox; version 3.3.0). 3D analysis was performed using

software CT Analyzer (version 1.18.8.0) or Amira 5.3 (Visage Imaging, Inc.).

2.15. Histologic and specialty staining

After μCT imaging, the retrieved subcutaneous masses and calvarial specimens were decalcified and subjected to paraffin embedding, followed by sectioning. The sections were deparaffinized and subjected to H & E staining (Solarbio, Cat# G1120), Masson trichrome staining (Solarbio, Cat#G1340), Modified Saffron-O and fast green stain kit (for bone; Solarbio, Cat#G1371) and Alcian blue staining (Solarbio, Cat# G2541) as described [83–87]. For immunohistochemical (IHC) staining, the tissue sections were deparaffinized, rehydrated, antigen-retrieval treated, blocked and incubated overnight with primary antibody against Collagen II (1:200 dilution; Abcam; Cat# ab307674), followed by stained with biotin-labeled goat anti-rabbit IgG and horseradish peroxidase-conjugated-labeled streptavidin. The staining results were recorded under a bright field microscope.

2.16. Next-generation RNA-sequencing analysis

Exponentially growing iMAD, iMEF, iCAL and imBMSC cells were infected with AdR-B9 or Ad-RFP for 48 h. Total RNA was isolated with the TRIZOL Reagent (Invitrogen, China) according to the manufacturer's protocol. RNA integrity was assessed using the Bioanalyzer 2100 system (Agilent Technologies, CA, USA). RNA-seq analysis was commercially conducted by BGI Genomics (Shenzhen, China). Briefly, 3 μg RNA per sample was used for library construction using NEBNext® UltraTM RNA Library Prep Kit for Illumina® (NEB, USA) following manufacturer's recommendations and index codes were added to attribute sequences to each sample. Library quality was assessed on the Agilent Bioanalyzer 2100 system. The clustering of the index-coded samples was performed on a cBot Cluster Generation System using TruSeq PE Cluster Kit v3-cBot-HS (Illumina) according to the manufacturer's instructions. After cluster generation, the libraries were sequenced on the Illumina Hiseq platform to generate 150 bp paired-end reads.

Raw data (raw reads) of Fastq format were initially processed through in-house perl scripts. Clean reads were obtained by removing reads containing adapters, ploy-N and low quality reads from raw data. At the same time, Q20, Q30 and GC contents of the clean data were calculated. The paired-end clean reads were aligned to the reference genome using Hisat2 v2.0.5. FeatureCounts v1.5.0-p3 was used to count the reads numbers mapped to each gene. Fragments Per Kilobase of transcript per Million mapped reads (FPKM) of each gene was calculated based on the length of the gene and reads count mapped to a given gene.

The sample matrix was collated using R (4.2.2). Specifically, the principal component analysis (PCA) of samples was performed using FactoMineR and factoextra packages, and the results were visualized by pca3d package. Differential expression analysis was performed using the edge R and limma packages. The Venn diagrams were drawn using the ggvenn package, and the clustering heatmap was drawn using the pheatmap package. Genes with $|\log_2 FC| > 1$ found by DESeq2 were designated as altered expressed genes, and with an adjusted P-value (FDR) < 0.05 were assigned as differentially expressed genes (DEGs). Gene Ontology (GO) enrichment analysis of DEGs was implemented by using the clusterProfiler package, and GO terms with FDR less than 0.05 were considered significantly enriched. The online KOBAS 3.0 program (http://kobas.cbi.pku.edu.cn/genelist/) was used to test the statistical enrichment of DEGs in KEGG pathways. The ggplot2 package was used to visualize the results in R. The KEGG terms with FDR <0.05 were considered significantly enriched.

2.17. Statistical analysis

Data were analyzed using GraphPad Prism 7 and presented as the mean ± standard deviations (SD). Statistical significance was determined by one-way analysis of variance and the student's *t*-test for the comparisons between groups. A value of $p < 0.05$ was considered statistically significant.

3. Results

3.1. The iMEF cells exhibit the highest proliferative activity, while imBMSC cells express the highest levels of stemness and mesoderm markers

While we previously demonstrated that iMAD, iMEF, iCAL and imBMSC cells are individually capable of differentiating into osteoblastic, chondrogenic, and adipogenic lineages [24–28], these MSCs derived from different tissues have never been compared directly for their progenitor characteristics and differential potential. Here, we first compared their morphologic characteristics and found their overall cellular morphology was rather similar (Fig. 1A). Cell proliferation assessed with crystal violet cell viability (Fig. 1B, panels *a* & *b*) and WST-1 assay (Fig. 1C) revealed that iMEF cells were most proliferative among the four MSC lines. TqPCR quantitative analysis revealed that, while the stemness markers, such as *CD90*, *CD105*, *Sox9*, *Tcl1*(Fig. S1A, panel a), and mesoderm markers, especially *Hand1*, and *Acta2* (Fig. S1A, panel b), were highly expressed in all four MSC lines, the stemness and mesoderm markers were significantly higher in imBMSC cells than that in other three MSC lines (Fig. 1D, panels a & **b)**. Interestingly, IF staining revealed CD105 and HAND1 were highly expressed only in imBMSC cells. NANOG was highly expressed in all four MSC lines, whereas ACTA2 was only highly expressed in iMEF cells (Fig. 1E & **S1B**). NC controls are shown in Fig. S1B. Collectively, these results demonstrate that the order of proliferation rate (from high to low) is iMEF > imBMSC ≥ iMAD > iCAL, whereas the expression levels of stemness and mesoderm markers (from high to low) were imBMSC > iMEF > iMAD > iCAL cells.

3.2. The iMAD cells exhibit the strongest osteogenic potential when induced by osteogenic medium or BMP9 in vitro

We first compared the osteogenic capacity of iMAD, iMEF, iCAL and imBMSC cells that were stimulated by osteogenic medium. ALP assay showed iMAD cells exhibited strong ALP staining at day 2, significantly earlier than other three MSC lines, although they also showed significant basal level of ALP staining (Fig. S2A). Quantitative ALP results also showed ALP activity in iMAD cells significantly increased at day 2, while peak ALP activities were shown for iCAL and imBMSC cells at day 7. Interestingly, iMAD and iCAL cells still had high ALP activity at day 12 (Fig. S2B). Alizarin red staining results revealed apparent matrix mineralization of iCAL at day 21, and for iMAD and imBMSC at day 28 (Fig. S2C). Through TqPCR analysis, early osteogenic marker (*Alp*), late osteogenic markers (*Ocn, Spp1* and *Col1a1*), and key regulators (*Runx2* and *Sp7*) were up-regulated in iMADs and imBMSCs by osteogenic medium for 3 days, especially for iMAD cells at day 1, while relatively weak up-regulation was found in iMEFs, and to lesser extent in iCALs (Fig. S3).

We next compared the osteogenic capacity of iMAD, iMEF, iCAL and imBMSC in response to osteogenic factor BMP9. Adenovirus-mediated overexpression of human BMP9 (Ad-B9) was confirmed by TqPCR analysis (Figs. S4A and B). Strong ALP staining in iMADs appeared at as early as day 2, and kept increasing at days 3 and 5 (Fig. 2A). For iCALs, apparent ALP staining was found at days 3 and 5, while robust ALP staining was detected at day 5 in iMEFs and imBMSCs (Fig. 2A). Consistent with the ALP staining results, quantitative ALP analysis showed ALP activities of all 4 lines significantly increased from days 2–5, most notably in iMAD cells (Fig. 2B). Alizarin red staining revealed apparent matrix mineralization nodules were formed in iMAD cells at as

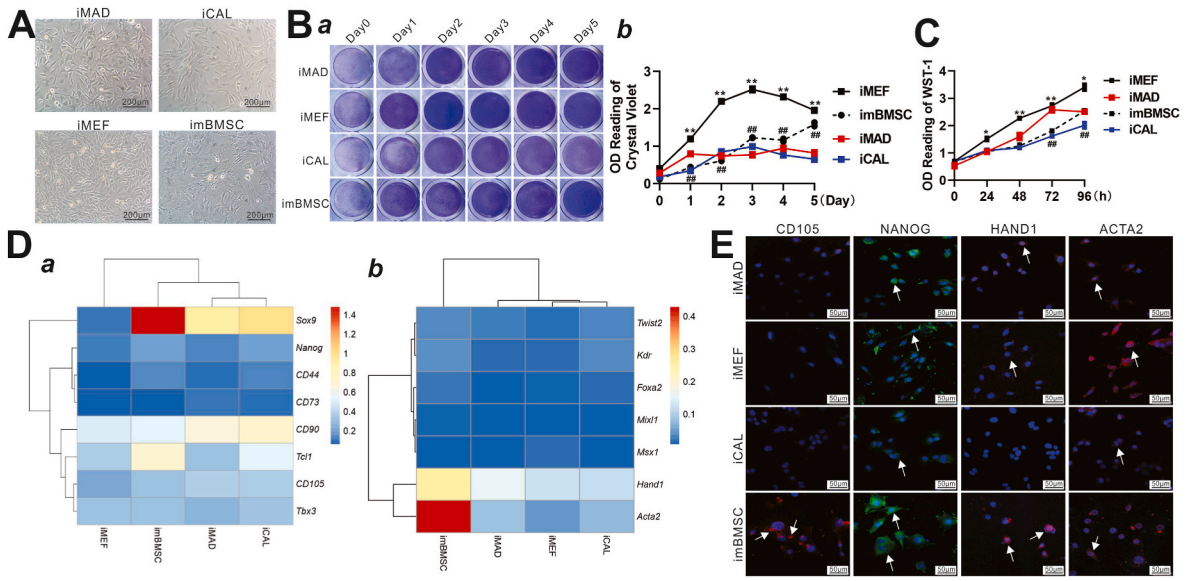

Fig. 1. Proliferative activity and the expression of characteristic stemness and mesoderm markers in the four types of MSC cells. (**A**) Morphological characteristics of iMAD, iMEF, iCAL and imBMSC cells (x100). Representative images are shown. (**B**) Crystal violet cell staining (***a***) and quantitative analysis (***b***) were used to assess cell viability of iMAD, iMEF, iCAL and imBMSC cells at Days 0, 1, 2, 3, 4 and 5. "**" $p < 0.01$, iMEF group *vs*. iCAL group, "##" $p < 0.01$, imBMSC group *vs*. iCAL group at the indicated time point. Representative images are shown. (**C**) WST-1 assay was used to assess cell proliferation of iMAD, iMEF, iCAL and imBMSC cells at 0, 24, 48, 72, and 96 h. "*" $p < 0.05$, "**"$p < 0.01$, iMEF group *vs*. iCAL group; "##"$p < 0.01$, imBMSC group *vs*. iCAL group. (**D**) Heatmap visualization of the expression of characteristic stemness genes (***a***) and mesoderm genes (***b***) in iMAD, iMEF, iCAL and imBMSC cells. (**E**) Immunofluorescence (IF) staining was used to assess the expression of NANOG (FITC-green), CD105 (APC-red), HAND1 (APC-red), ACTA2 (APC-red) in iMAD, iMEF, iCAL, and imBMSC cells, while cell nuclei were counterstained with DAPI (blue) (x400). Representative positive stains are indicated with white arrows. Representative images are shown.

early as day 9, in iMEF and iCAL cells at day 21, and in imBMSC cells at day 28 (Fig. 2C). TqPCR analysis also indicated that the osteogenesis-related marker genes were mostly upregulated by BMP9 to varying degrees at the tested timepoints (Fig. S5). Clustering analysis showed that osteogenesis-related genes were most significantly up-regulated by BMP9 in iMAD cells as early as at day 1, while the gene expression levels were least affected by BMP9 in iMEFs at day 3 (Fig. 2D). Collectively, these results strongly suggest a ranking order of *in vitro* osteogenic capability induced by osteogenic medium or BMP9: iMAD > iCAL > imBMSC ≥ iMEF.

3.3. The iMAD cells are most adipogenic upon BMP9 stimulation in vitro

We further compared the adipogenic capacity of iMAD, iMEF, iCAL and imBMSC cells induced by BMP9. Adenovirus-mediated overexpression of mouse BMP9 (AdR-B9) were verified in all 4 cell lines (Figs. S6A and B). Oil red O (Fig. 3A, panel a) and Bodipy 493/503 staining (Fig. 3A, panel b) showed that AdR-B9 effectively induced the formation of lipid droplets in iMAD and imBMSC cells at day 3, and in iMEF and iCAL cells at day 5. TqPCR analysis of the key adipogenesis regulatory genes (*Pparγ and Cebpa*) and the late adipogenic gene *Lpl* were mostly upregulated in the four cell lines, although *Pparγ* in iMAD, *Cebpa* in imBMSC and iMEF, and *Lpl* in iCAL were not significantly upregulated (Fig. S7A). Clustering analysis indicated the expression patterns of these adipogenesis markers are significantly different in iMAD at day 1, iMEF at day 2, and iMAD and imBMSC at day 3 (Fig. 3B). IF staining also revealed that the expression of PPARγ was increased in all 4 MSC lines, especially in iMAD and imBMSC cells (Fig. S7B), compared with that in the negative control (Fig. S7B). Collectively, the above results strongly suggest that the ranking order of adipogenic capability induced by BMP9 may be iMAD ≥ imBMSC > iMEF ≥ iCAL cells *in vitro*.

3.4. The iMAD cells exhibit the strongest osteogenic and adipogenic capability in subcutaneous ectopic bone formation model

Subconfluent iMAD, iMEF, iCAL and imBMSC cells were infected with Ad-B9 or Ad-GFP, and injected subcutaneously into the flanks of athymic nude mice. After 4 weeks, the mice were euthanized; and subcutaneous masses were retrieved in the Ad-B9 groups. Consistent with our previous reports [24–28], no bony masses were detected in Ad-GFP groups. The μCT imaging analysis revealed that, while all 4 types of MSC lines formed bone subcutaneously, but the sizes of the masses varied significantly (Fig. 4A, panel a & b). The μCT quantitative analysis showed that the mean bone density, tissue volume (TV), bone volume (BV), BV/TV of iMAD, iCAL, and imBMSC cells were higher than those of iMEF, except BV and BV/TV of iMAD, BV and TV of iCAL. The trabecular number (Tb. N) was increased in iMAD cells, compared to iMEF cells. Compared with iMAD, the trabecular thickness (Tb. Th) of iCAL and imBMSC cells was increased, while trabecular separation (Tb. Sp) of iMEF was decreased; and Tb. Sp of iCAL and imBMSC decreased to a greater extent and were much lower than iMEF (Fig. 4A, panel c). H & E staining showed that apparent bone and/or cartilage formation was found in all 4 types of MSCs (Fig. 4B, panel a). Masson trichrome staining revealed that significantly mature bone matrix was formed in the iMAD and iCAL groups, as well as in imBMSC group, but noticeably weak or absent in iMEF group (Fig. 4B, panel b). Safranin O and fast green staining revealed that significantly mature bone formation was presented in iMAD and iCAL groups, compared with a much lesser extent in iMEF and imBMSC groups (Fig. 4B, panel c). IHC staining of collagen II showed that cartilage formation was found in all 4 types of MSCs, especially in iMEF group (Fig. 4B, panel d). Alcian blue staining showed that apparent cartilage formation was observed in imBMSC and iMEF groups, but to a much lesser extent in iMAD and iCAL groups (Fig. S8A). Furthermore, Oil red O staining indicated that lipid droplet accumulation was mostly pronounced in iMAD group, to a much lesser extent in iMEF and imBMSC groups, but almost absent in iCAL group (Fig. S8B). Collectively, these *in vivo* results demonstrate that, while all 4 types of MSC lines have osteogenic, chondrogenic and adipogenic differentiation upon BMP9 stimulation, these lines exhibited distinctly different osteogenic and adipogenic potential. Our *in vivo* results indicate that the ranking of osteogenic ability is iMAD ≥ iCAL > imBMSC > iMEF cells, while the ranking of adipogenic capability is iMAD ≥ imBMSC > iMEF

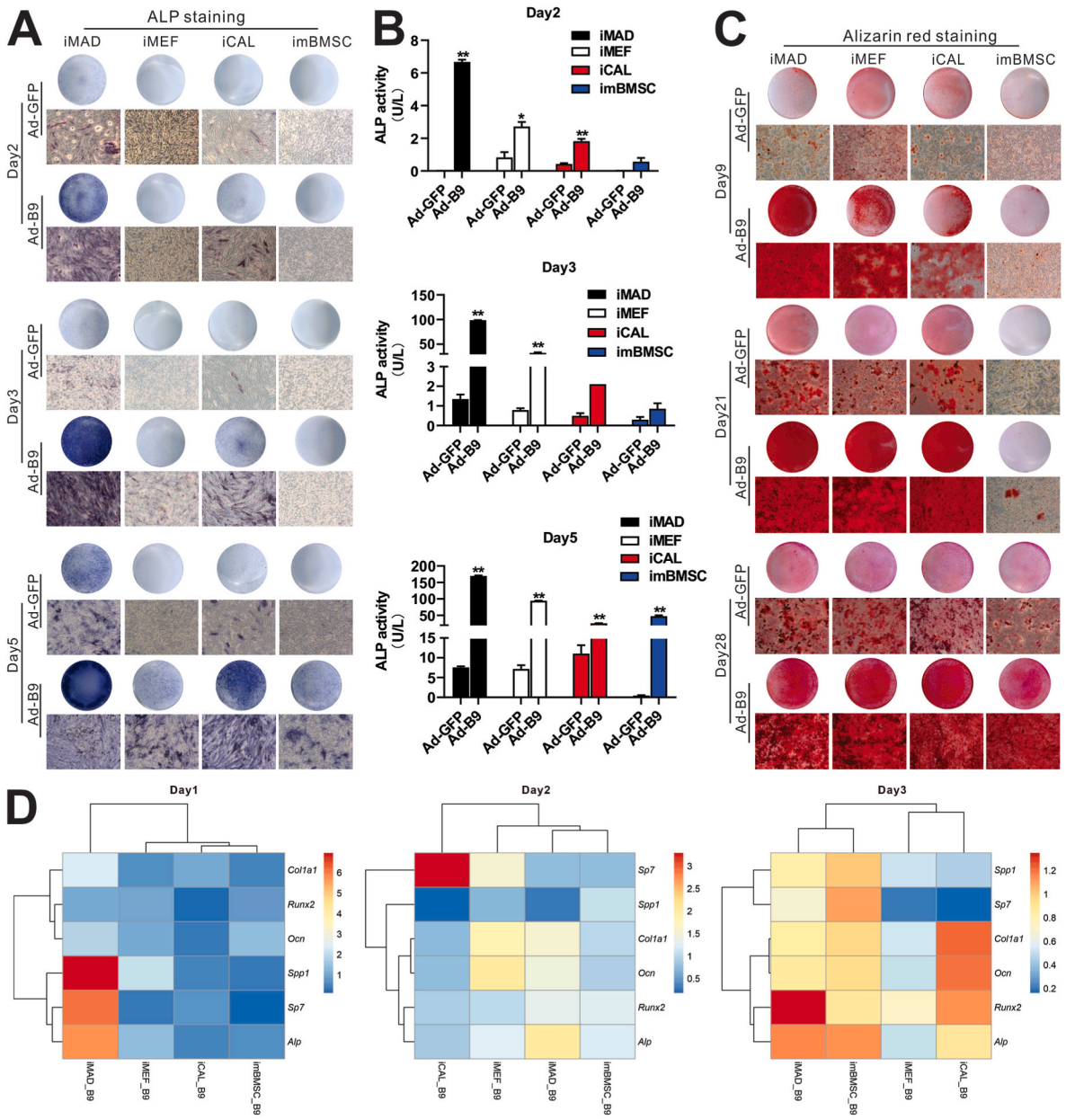

Fig. 2. Osteogenic activities of the four types of MSC cells induced by BMP9 *in vitro*. Subconfluent iMAD, iMEF, iCAL and imBMSC cells were infected with Ad-B9 or Ad-GFP, respectively. (**A**) ALP staining was determined at days 2, 3 and 5, respectively. Representative images are shown. (**B**) ALP activity was tested at days 2, 3 and 5 respectively. "*" $p < 0.05$, "**" $p < 0.01$, Ad-B9 group *vs.* Ad-GFP group at the indicated time point. (**C**) Alizarin red staining was done at days 9, 21 and 28, respectively. Representative images are shown. (**D**) Heatmap visualization of the expression of osteogenic markers and regulatory genes induced by BMP9 at days 1, 2,and 3, respectively. Representative images are shown.

≥ iCAL cells.

3.5. The iMAD cells provide the most optimal repair of mouse cranial defect among the four types of MSC lines transduced by BMP9

Using one of the most rigorous bone repair animal models [27,78], we further tested the cranial defect healing effect of the 4 types of MSC lines transduced with BMP9. In order to provide a 3D environment for effective bone regeneration, we employed the GelMA hydrogels that were shown to support the survival, proliferation, and osteogenic differentiation of stem or progenitor cells [88,89]. We tested different GelMA concentrations, cell numbers (10^5 or 10^6 cells), and UV-crosslinking duration (Fig. S9A, panels *a* & ***b***) and found that 5 % GelMA and 30 s UV-crosslinking provided optimal cell viability (Fig. S9B, panels *a-c*), leading to the 5 % GelMA+10^6 cells mixture preparations of iMAD, iMEF, iCAL, and imBMSC cells transduced with Ad-B9 or Ad-GFP for implantation into the calvarial defects of athymic nude mice (Fig. S9C).

Using the above optimized conditions, we implanted the Ad-B9 or Ad-GFP transduced MSCs mixed with 5 % GelMA hydrogel into the mouse calvarial defects. The animals were sacrificed after 4 weeks, and the retrieved cranial samples were subjected to microCT imaging. As shown in Fig. 5A panel a, the cranial defects in the iMAD and iCAL groups were almost completely repaired, while significant defects remained in the iMEF and imBMSC groups. Quantitative analysis of the μCT data showed the bone mineral density(BMD), BV and BV/TV of iCAL and iMAD groups were in general higher than that in iMEF and imBMSC groups. Furthermore, the Tb.N of the iMAD and iCAL groups were also higher than that in the iMEF and imBMSC groups, in which the iMEF group had the least number, and Tb.Sp was significantly lower in

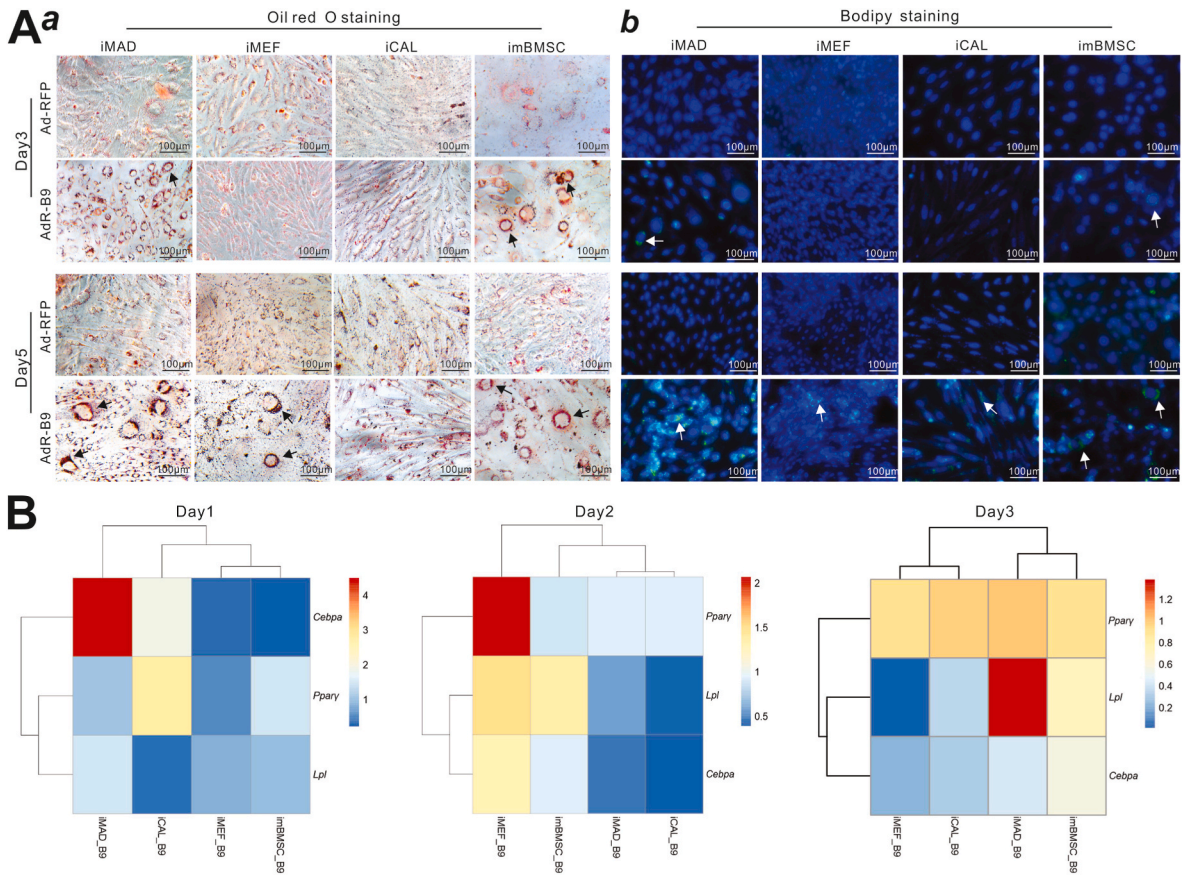

Fig. 3. Adipogenic activities of the four types of MSC cells induced by BMP9 *in vitro*. Subconfluent iMAD, iMEF, iCAL and imBMSC cells were infected with AdR-B9 or Ad-RFP, respectively. (**A**) Oil red O staining (***a***) and Bodipy 493/503 staining (***b***) were done at day 3 and 5, respectively. Representative lipid droplets were indicated with arrows (x200). Representative images are shown. (**B**) Heatmap visualization of the expression of adipogenic regulatory and marker genes induced by BMP9 at day 1, 2, and 3, respectively. Representative images are shown.

iCALs compared with that in iMEFs and imBMSCs (Fig. 5A, panel b). As expected, no significant bone healing of the cranial defects was found in the four MSC lines transduced with Ad-GFP (data not shown).

H & E histologic analysis showed that the iMAD and iCAL groups exhibited significant new bone formation that almost covered the cranial defect area from edge to edge, while fibrous tissue formation at the defect site was observed in the iMEF group, and cartilaginous repair was found in the imBMSC group (Fig. 5B, panel a). Masson trichrome staining analysis indicated that robust and mature bone was found in the iMAD group, and a lesser extent, in the iCAL group, whereas fibrous and cartilaginous tissues were observed in the iMEF and imBMSC groups, respectively (Fig. 5B, panel b). Safranin O and fast green staining revealed that, at the center of the healing site, more mature bone was found in the iMAD and iCAL groups, to a lesser extent in the imBMSC group, but least extent in the iMEF group (Fig. 5B, panel c). IHC staining of collagen II and Alcian blue staining further showed that cartilage formation was found at the center of the healing sites in all 4 types of MSCs (Fig. S9D). Taken together, these results demonstrate that the ranking of bone regeneration ability to repair calvarial defect may be iCAL and iMAD > imBMSC > iMEF cells *in vivo*. Given the fact that iCAL cells are not readily available due to limitations in processing and yield, iMAD cells may represent one of the best sources of MSC progenitors for bone tissue engineering.

3.6. MSC cells derived from four tissue sources exhibit an overlapping yet distinct transcriptomic landscape during BMP9-induced osteogenic differentiation

To understand the underlying mechanisms of BMP9-mediated osteogenic differentiation among iMAD, iMEF, iCAL, and imBMSC cells, we conducted RNA-seq transcriptomic analysis upon BMP9 stimulation. PCA showed that, while the individual transcriptome varied significantly, they had a tendency to aggregate upon BMP9 stimulation (Fig. 6A), suggesting that BMP9 may induce overlapping transcriptomic responses in the MSC lines derived from four different tissue sources. We further identified a total of 2508 differentially expressing genes (DEGs) in the four MSC lines. Venn diagram analysis indicated that there are 26 up-regulated DEGs and 24 down-regulated DEGs shared by the four MSC lines (Fig. 6B), which could be further clustered based on the DEGs' expression changes (Fig. S10). Not surprisingly, several of the common DEGs, such as *Hey1*, *Id1*, *Id2*, *Id4*, *Smad6*, *Fgfr3*, *Pparg*, *Dlx2*, and *Tgfb1*, were previously identified as the downstream targets of BMP9 signaling in MSCs [90–93]. Among the four MSC lines, iCAL cells had the most numbers of DEGs, 826 up-regulated and 1125 down-regulated DEGs, while imBMSC cells had 237 up-regulated and 191 down-regulated DEGs; iMAD cells had 193 up-regulated and 216 down-regulated DEGs; and iMEF cells had 194 up-regulated and 207 down-regulated DEGs (Fig. 6B). These transcriptomic analysis results demonstrate that the four MSC lines undergo osteogenic differentiation by regulating overlapping but distinct target genes.

Cluster analysis of the DEGs revealed that while iCAL cells exhibited a rather distinct pattern of DEGs during BMP9-induced osteogenic differentiation, iMAD, iMEF and imBMSC cells shared a significantly overlapping expression pattern of DEGs upon BMP9 stimulation (Fig. 6C). Gene ontology enrichment analysis of the top 50 biological processes (Fig. S11A) identified several top enriched processes that are associated with osteogenesis in all four MSC lines, including blood vessel morphogenesis, angiogenesis and vasculature development as well as

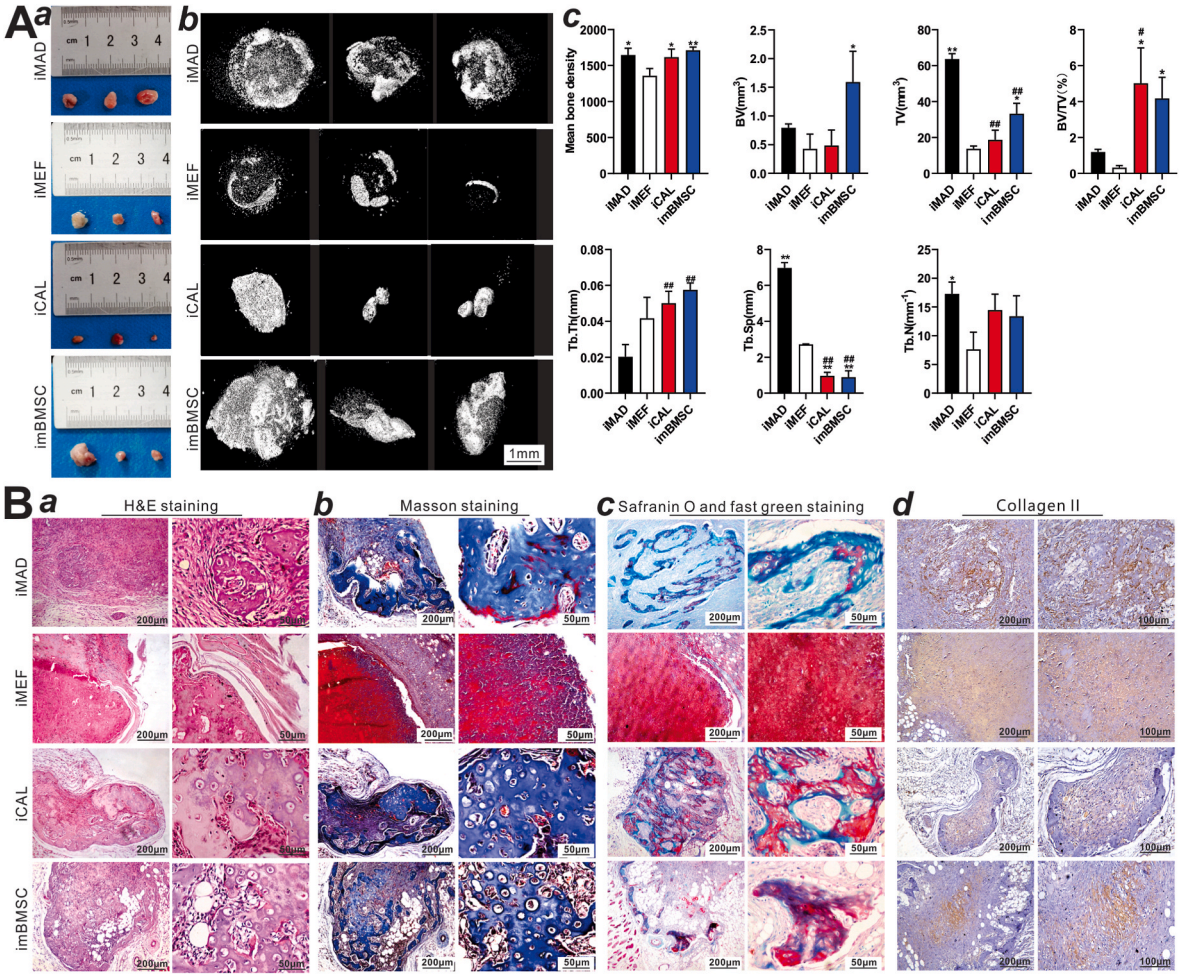

Fig. 4. Osteogenic and chondrogenic activities of the four types of MSCs induced by BMP9 *in vivo*. Subconfluent iMAD, iMEF, iCAL and imBMSC cells were infected with Ad-B9 for 36 h, collected and injected into the flanks of athymic nude mice subcutaneously. (**A**) At 4 weeks after implantation, the subcutaneous masses were retrieved (***a***), and subjected to μCT imaging (***b***). Representative images are shown. The bone formation quantitative parameters of the ectopic bone masses were analyzed (***c***). "*" $p < 0.05$, "**" $p < 0.01$, iMEF *vs.* iMAD, iCAL and imBMSC, respectively. "#" $p < 0.05$, "##" $p < 0.01$, iMAD vs. iMEF, iCAL and imBMSC, respectively (***c***). (**B**) Subcutaneous masses were subjected to H & E staining (***a***), Masson Trichrome staining (***b***), Safranin O and fast green staining (***c***) and anti-type II collagen staining (***d***)(100x and 200x or 400x). Representative images are shown.

more osteogenic differentiation processes enriched in iMAD, iMEF and imBMSC cells (Fig. 6D). KEGG pathway analysis of the top 35 enriched signaling pathways in the four MSC lines (Fig. S11B) revealed the enrichment of osteogenesis-related signaling pathways in most or all four MSC lines, including Wnt signaling pathways (except imBMSC), TGF-β signaling pathways (except iCAL), PI3K-AKT signaling pathways, MAPK signaling pathways, Hippo signaling pathways. Furthermore, the JAK-STAT signaling pathway was enriched in iMAD cells (Fig. 6E). Further clustering analysis of the DEGs enriched in the above osteogenesis-related KEGG pathways indicates that iMAD, iMEF and imBMSC cells shared a more closely related and overlapping expression profiles, whereas iCAL cells displayed a rather distinct expression profile from the other three MSC lines (Fig. 6F), which may underly potential fundamental differences related to tissue sources. Nonetheless, the above transcriptomic analyses demonstrate that MSC lines derived from the four tissue sources can undergo effective osteogenic differentiation by regulating a panel of overlapping yet distinct genes related to osteogenesis signaling pathways.

4. Discussion

While autogenous bone graft remains the gold standard to promote bone healing, bone tissue engineering based on bone progenitor cells with osteogenic factors represents a promising approach [2–4]. Since embryonic stem cells (ESCs) and iPSCs are not widely used due to ethical issues and challenging genetic manipulation, other sources of bone progenitor cells or MSCs are highly sought after. Numerous studies focused on the use of bone marrow-derived stem cells or adipose-derived stem cells (ADSCs) in bone regeneration [5–8,94], while calvarial suture-derived stem cells were reported that have intrinsic bone reparative potential [95]. Nonetheless, the osteogenic activity and bone defect repair efficiency have never been compared among different sources of MSCs.

In this study, we conducted a comprehensive comparative analysis of the bone regeneration potential for MSCs derived from four different tissue sources, including prototypical MSCs: mouse embryonic fibroblasts (iMEFs), mouse bone marrow-derived mesenchymal stem cells (imBMSCs), mouse adipose-derived mesenchymal stem cells (iMADs), and mouse calvarial suture-derived mesenchymal stem cells (iCALs) [24–28]. While the four MSC lines were immortalized, we previously demonstrated that the immortalization is reversible; and all four lines retain MSC multipotency and can undergo osteogenic, chondrogenic and adipogenic differentiation under proper stimuli [24,29–34]. Thus, these lines provide a unique platform to compare the optimal osteogenic capacity of different tissue-derived MSCs in a comprehensive fashion. Ultimately, this line of investigation can enable us to use the optimal

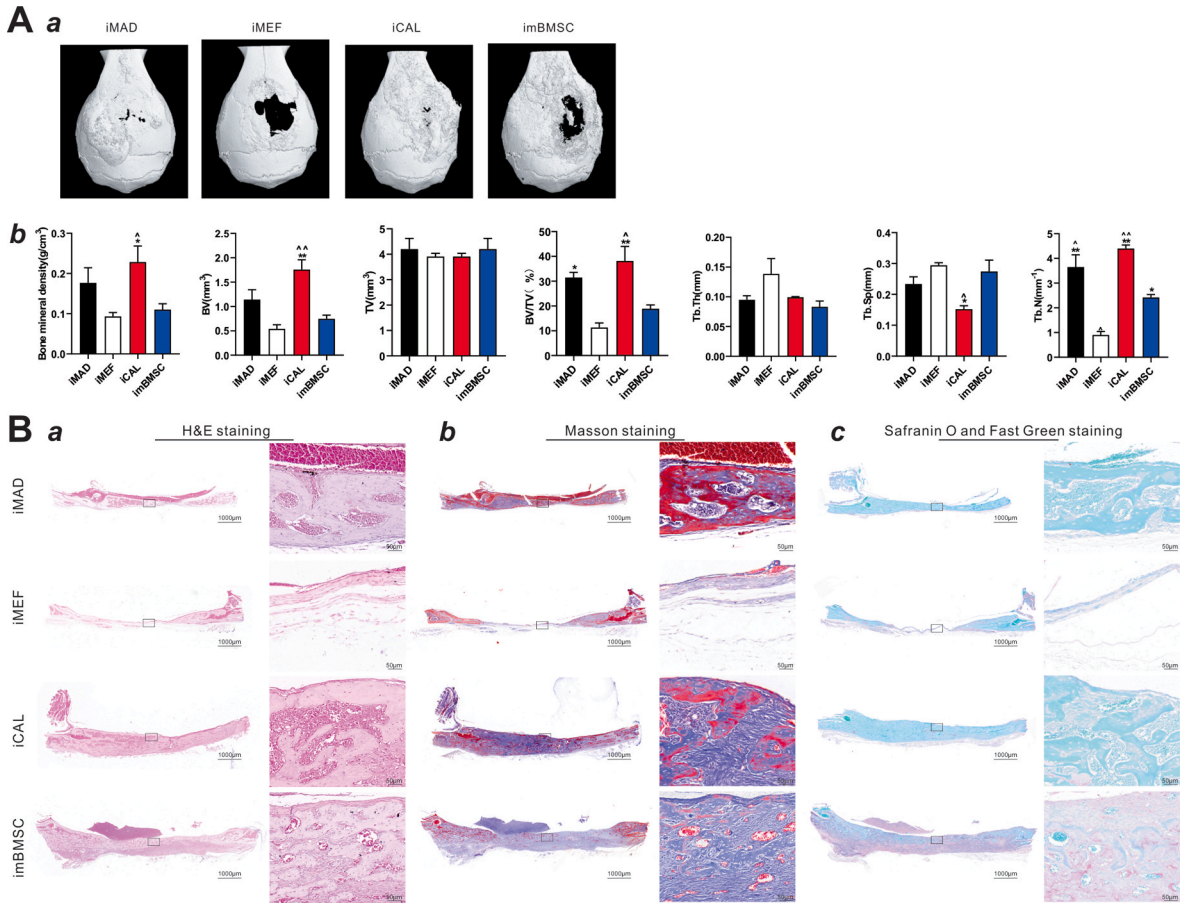

Fig. 5. Differential repair efficiencies of mouse calvarial defects among the four types of MSCs transduced by BMP9 laden in GelMA hydrogel. Subconfluent iMAD, iMEF, iCAL and imBMSC cells were infected with Ad-B9 or Ad-GFP for 36 h, collected and resuspended in 5 % GelMA hydrogel. Meanwhile, mouse calvarial defect model was created as described in the Methods. The cell-laden hydrogel was added to the defects, followed by photo-crosslinking. (**A**) At 4 weeks, the mice were sacrificed and the calvarial samples were retrieved and fixed for the μCT imaging (***a***), and the bone related parameter were analyzed (***b***). No apparent defect repair was observed in the Ad-GFP-transduced cells groups (data not shown). "*" $p < 0.05$, "**" $p < 0.01$, iMEF *vs.* iMAD, iCAL and imBMSC, respectively. "^" $p < 0.05$, "^^" $p < 0.01$, imBMSC *vs.* iMAD, iCAL and iMEF cells, respectively (***b***). (**B**) The calvarial defect repair sample were fixed, decalcified, and subjected to H & E staining (***a***), Masson trichrome staining (***b***), and Safranin O and fast green staining (***c***)(20x and 400x). Representative images are shown.

progenitor sources for bone tissue engineering.

In this study, we demonstrated that the iMEF cells had the highest proliferative activity, compared with that of iMAD, iCAL and imBMSC cells. Nonetheless, all four lines expressed high levels of mesoderm and stemness markers, such as *CD90*, *CD105*, *Sox9*, *Tcl1*, *Hand1*,and *Acta2*. Interestingly, our results indicate that imBMSC, but not iMEF, cells exhibited the highest expression levels of stemness and mesoderm markers, compared with other three MSC lines.

While all four MSC lines could differentiate into multiple lineages, we compared the osteogenic and adipogenic capacities of the four lines induced by osteogenic medium or BMP9 through *in vitro* osteogenic assays, subcutaneous ectopic ossification model, and a critical-sized mouse calvarial defect repair model. Our results indicated that iMAD and iCAL cells had stronger osteogenic ability, and iMAD and imBMSC cells were prominent in adipogenesis. Considering the accessibility and availability, our findings strongly suggest that adipose-derived iMAD cells may be a preferred progenitor source for cell-based bone tissue engineering. It is noteworthy that we utilized GelMA hydrogel as a cell delivery vehicle in the calvarial defect repair study as GelMA hydrogel, also called photo-cross-linkable gelatin, is known to exhibit excellent biocompatibility, biodegradability and moldability, and has been used in biomedical applications such as wound dressings, cartilage regeneration, and bone regeneration [76,88,89].

In addition to the four types of MSC lines, other types of MSCs have been investigated for bone regeneration. For example, periosteal cells, $Gli1^+$ suture stem cells (SuSCs), dental pulp MSCs (DPSCs), gingival MSCs (GMSCs), human umbilical cord-derived stem cells (hUC-MSCs), and human amniotic mesenchymal stromal cells (HAMSCs) were shown to induce bone regeneration [65,74,96,97]. Interestingly, a significant number of studies were carried out to compare the bone regenerative capacity between BMSCs and ADSCs, and the outcomes were somewhat contradictory. Xu et al. compared the human BMSCs and adipose tissue-derived MSC (ATSCs), and reported that BMSCs possessed stronger osteogenic and lower adipogenic differentiation potentials compared to ATSCs [98]. Consistent with our findings, Zhou et al. reported that ADSCs showed lower transcriptomic heterogeneity and higher proliferative activity and senescent tolerance, meaning that ADSCs may be more suitable for cell transplantation treatments such as osteoarthritis treatment [99]. Li et al. focused on exosomes or small extracellular vesicles (EVs) of ADSCs, BMSCs, and synovial mesenchymal stem cells (SMSCs) and found that the ADSC-EVs has stronger chondrogenic and osteogenic capacities *in vitro* and *in vivo* [100]. Nonetheless, contradictory findings have been reported, and no comprehensive comparative studies had ever been conducted prior to our current study. Furthermore, our findings provide valuable justification for the potential preclinical and clinical use of adipose-derived MSCs to treat non-unions or large bony defect [101–105].

To further understand the potential mechanism underlying the distinct osteogenic capability of the four MSC lines, we performed RNA sequencing and analyzed the transcriptomic landscapes of the iMAD,

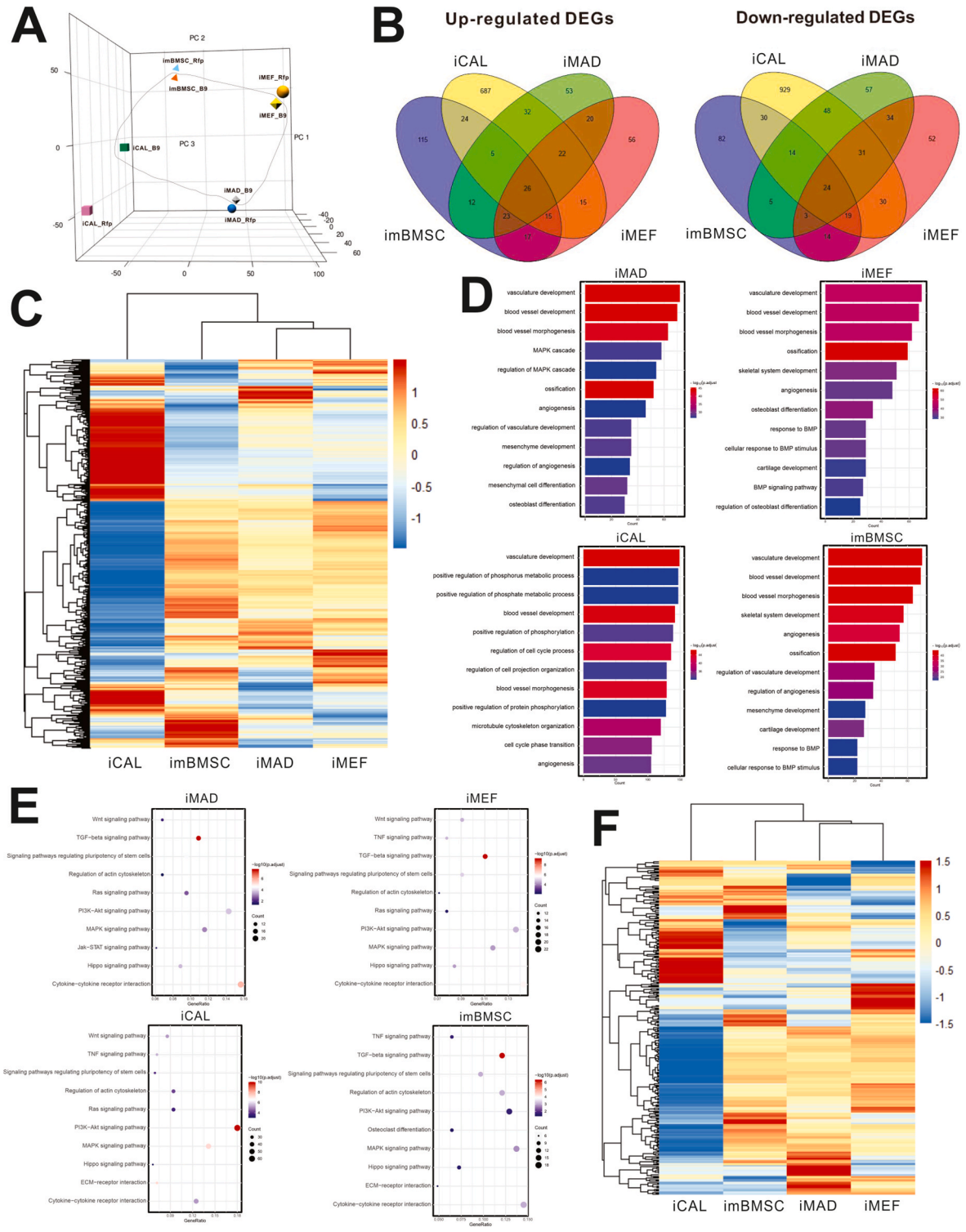

Fig. 6. The transcriptomic landscape of the four types of MSCs stimulated by BMP9. Subconfluent iMAD, iMEF, iCAL and imBMSC cells were infected with AdR-B9 or Ad-RFP for 48 h. Total RNA was collected for RNA-seq analysis. (**A**) Principal component analysis (PCA) and 3D visualization. (**B**) Venn Diagram of the differentially expressed genes (DEGs). (**C**) Clustering analysis of 2508 genes with differential expression. (**D**) GO enrichment of top 12 biological processes related to osteogenesis. (**E**) KEGG analysis of top 10 signaling pathways associated with differentiation. (**F**) Clustering analysis of major signaling pathway genes enriched in Fig. 6E.

iMEF, iCAL, and imBMSC cells that were stimulated with BMP9. Our results revealed that the four lines shared extensively overlapping patterns of DEGs. Interestingly, several of the common DEGs, such as *Hey1*, *Id1*, *Id2*, *Id4*, *Smad6*, *Fgfr3*, *Pparg*, *Dlx2*, and *Tgfb1*, were previously identified as the downstream targets of BMP9 signaling in MSCs [90–93]. Clustering and pathway analyses indicated that iMAD, iMEF and imBMSC transcriptomes shared similar expression patterns and osteogenic differentiation processes, which were significantly different from that in iCAL cells. Nonetheless, all or most of the four MSC lines enriched multiple osteogenesis-related pathways, such as Wnt, TGF-β,

PI3K/AKT, MAPK, Hippo and JAK-STAT signaling pathways [11,15,16,93]. These transcriptomic results reveal that, upon BMP9 stimulation, the four MSC lines undergo osteogenic differentiation by regulating overlapping but distinct target genes. It is noteworthy that RNA-seq is a cross-sectional snapshot of the transcriptomic changes during the early stage of osteogenic differentiation. While it is conceivable that more meaningful data can be obtained if a multiple timepoint longitudinal RNA-seq analysis is conducted, we have demonstrated that upon osteogenic stimulations, iMAD cells exhibited highest abilities to induce early and late osteogenic markers *in vitro*, and induced most robust subcutaneous bone formation and cranial defect repair *in vivo*. Therefore, by taking the following features into account, easy access and availability, decent *in vitro* proliferative activity, and robust *in vivo* osteogenic capability, we conclude that adipose-derived MSCs represent a superior progenitor cell source for cell-based bone tissue engineering.

In summary, we systematically compared the proliferative and osteogenic characteristics of MSC cells derived from four different tissue sources in order to identify an optimal progenitor cell source for cell-based bone tissue engineering. Our results indicated that adipose-derived MSCs (iMAD) and cranial suture-derived MSCs (iCAL) exhibited highest osteogenic capability in heterotopic osteogenesis and calvarial defect repair. Transcriptomic analysis revealed the similarities and distinct differences that underly molecular mechanisms governing osteogenic differentiation of the four MSC lines. Taking account of the abundance and accessibility, we believe adipose-derived MSCs represent the best cell choice for cell-based bone tissue engineering applications. Nonetheless, our current study has limitations. We need to conduct similar studies using primary MSCs, and more importantly to validate these findings using human MSCs. Ultimately, we will explore the potential use of human adipose-derived MSC-based bone tissue engineering to treat nonunion and/or large bony defects in clinical settings.

5. Conclusion

To identify an optimal progenitor cell source for bone tissue engineering applications, we conducted a comprehensive comparative analysis of the proliferative activity and differentiation potential of four commonly used MSC sources including mouse embryonic fibroblasts (iMEF), mouse bone marrow stromal stem cells (imBMSC), mouse calvarial mesenchymal progenitors (iCAL), and mouse adipose-derived mesenchymal stem cells (iMAD). Our results showed that iMEFs had the highest proliferation rate, while imBMSCs expressed the highest level of stemness and mesoderm markers *in vitro*. The iMAD exhibited the strongest osteogenic and adipogenic capabilities upon BMP9 stimulation *in vitro*. In vivo studies employing ectopic osteogenesis and critical-sized calvarial defect repair model revealed that iMAD and iCAL cells exhibited the highest osteogenic capability. Transcriptomic analysis indicated that, while each MSC line regulated a distinct set of DEGs, all four MSC lines underwent osteogenic differentiation through several common signaling pathways including Wnt, TGF-β, PI3K/AKT, MAPK, Hippo and Jak-STAT signaling pathways. Collectively, our results demonstrate that adipose-derived MSCs represent the best seed cells of choice for cell-based bone tissue engineering applications.

Ethics approval and consent to participate

The reported work follows the guidelines approved by all relevant institutional ethics committees. All of the authors consented to participate in the reported work.

CRediT authorship contribution statement

Yannian Gou: Conceptualization, Data curation, Formal analysis, Methodology, Validation, Visualization, Writing – original draft, Writing – review & editing. **Yanran Huang:** Data curation, Formal analysis, Project administration, Writing – original draft, Writing – review & editing. **Wenping Luo:** Data curation, Formal analysis, Methodology, Writing – original draft, Writing – review & editing. **Yanan Li:** Data curation, Formal analysis, Methodology, Resources, Writing – review & editing. **Piao Zhao:** Data curation, Methodology, Resources, Writing – review & editing. **Jiamin Zhong:** Data curation, Investigation, Methodology, Resources, Writing – review & editing. **Xiangyu Dong:** Formal analysis, Methodology, Resources, Validation, Writing – review & editing. **Meichun Guo:** Methodology, Resources, Writing – review & editing. **Aohua Li:** Data curation, Formal analysis, Methodology, Resources, Writing – review & editing. **Ailing Hao:** Formal analysis, Methodology, Resources, Validation, Writing – review & editing. **Guozhi Zhao:** Methodology, Resources, Validation, Writing – review & editing. **Yonghui Wang:** Investigation, Methodology, Resources, Validation, Writing – review & editing. **Yi Zhu:** Formal analysis, Methodology, Resources, Validation, Writing – review & editing. **Hui Zhang:** Methodology, Resources, Validation, Writing – review & editing. **Yunhan Shi:** Methodology, Resources, Validation, Writing – review & editing. **William Wagstaff:** Methodology, Resources, Validation, Writing – review & editing. **Hue H. Luu:** Conceptualization, Funding acquisition, Resources, Supervision, Writing – original draft, Writing – review & editing. **Lewis L. Shi:** Formal analysis, Funding acquisition, Supervision, Writing – original draft, Writing – review & editing. **Russell R. Reid:** Conceptualization, Formal analysis, Funding acquisition, Project administration, Supervision, Writing – original draft, Writing – review & editing. **Tong-Chuan He:** Conceptualization, Data curation, Formal analysis, Funding acquisition, Methodology, Project administration, Resources, Supervision, Validation, Writing – original draft, Writing – review & editing. **Jiaming Fan:** Conceptualization, Data curation, Formal analysis, Funding acquisition, Methodology, Project administration, Resources, Supervision, Validation, Writing – original draft, Writing – review & editing.

Declaration of competing interest

The authors declare they have no competing interests.

Acknowledgements

The reported study was supported in part by research grants from the Natural Science Foundation of China (82102696 to JF), the Chongqing Bayu Young Scholar Award (JF), the 2019 Chongqing Support Program for Entrepreneurship and Innovation (No. cx2019113 to JF), the 2019 Funding for Postdoctoral Research (Chongqing Human Resources and Social Security Bureau No.298 to JF), and the National Institutes of Health (CA226303 to TCH, and DE030480 to RRR). WW was supported by the Medical Scientist Training Program of the National Institutes of Health (T32 GM007281). This project was also supported in part by The University of Chicago Cancer Center Support Grant (P30CA014599) and the National Center for Advancing Translational Sciences of the National Institutes of Health through Grant Number UL1TR002389-07. TCH was also supported by the Mabel Green Myers Research Endowment Fund and The University of Chicago Orthopaedics Alumni Fund. Funding sources were not involved in the study design, in the collection, analysis and interpretation of data, in the writing of the report, and in the decision to submit the paper for publication.

Appendix A. Supplementary data

Supplementary data to this article can be found online at https://doi.org/10.1016/j.bioactmat.2023.12.003.

References

[1] B.R. Olsen, A.M. Reginato, W. Wang, Bone development, Annu. Rev. Cell Dev. Biol. 16 (1) (2000) 191–220.
[2] A. Salhotra, H.N. Shah, B. Levi, M.T. Longaker, Mechanisms of bone development and repair, Nat. Rev. Mol. Cell Biol. 21 (11) (2020) 696–711.

[3] C. Myeroff, M. Archdeacon, Autogenous bone graft: donor sites and techniques, J. Bone Joint Surg. Am. 93 (23) (2011) 2227–2236.
[4] H.S. Sohn, J.K. Oh, Review of bone graft and bone substitutes with an emphasis on fracture surgeries, Biomater. Res. 23 (2019) 9.
[5] M.F. Pittenger, D.E. Discher, B.M. Peault, D.G. Phinney, J.M. Hare, A.I. Caplan, Mesenchymal stem cell perspective: cell biology to clinical progress, NPJ Regen. Med. 4 (1) (2019) 22.
[6] F. Rastegar, D. Shenaq, J. Huang, et al., Mesenchymal stem cells: molecular characteristics and clinical applications, World J. Stem Cell. 2 (4) (2010) 67–80.
[7] M. Bartold, S. Gronthos, D. Haynes, S. Ivanovski, Mesenchymal stem cells and biologic factors leading to bone formation, J. Clin. Periodontol. 46 (Suppl 21) (2019) 12–32.
[8] C.M. Teven, X. Liu, N. Hu, et al., Epigenetic regulation of mesenchymal stem cells: a focus on osteogenic and adipogenic differentiation, Stem Cell. Int. 2011 (2011), 201371.
[9] H.H. Luu, W.X. Song, X. Luo, et al., Distinct roles of bone morphogenetic proteins in osteogenic differentiation of mesenchymal stem cells, J. Orthop. Res. 25 (5) (2007) 665–677.
[10] M. Pakvasa, A. Alverdy, S. Mostafa, et al., Neural EGF-like protein 1 (NELL-1): signaling crosstalk in mesenchymal stem cells and applications in regenerative medicine, Genes Dis. 4 (3) (2017) 127–137.
[11] S. Mostafa, M. Pakvasa, E. Coalson, et al., The wonders of BMP9: from mesenchymal stem cell differentiation, angiogenesis, neurogenesis, tumorigenesis, and metabolism to regenerative medicine, Genes Dis. 6 (3) (2019) 201–223.
[12] X. Huang, Q. Chen, W. Luo, et al., SATB2: a versatile transcriptional regulator of craniofacial and skeleton development, neurogenesis and tumorigenesis, and its applications in regenerative medicine, Genes Dis. 9 (1) (2022) 95–107.
[13] J. Liao, B. Chen, Z. Zhu, et al., Long noncoding RNA (lncRNA) H19: an essential developmental regulator with expanding roles in cancer, stem cell differentiation, and metabolic diseases, Genes Dis. 10 (4) (2023) 1351–1366.
[14] A. Weiss, L. Attisano, The TGFbeta superfamily signaling pathway, Wiley Interdiscip. Rev. Dev. Biol. 2 (1) (2013) 47–63.
[15] K. Qin, M. Yu, J. Fan, et al., Canonical and noncanonical Wnt signaling: multilayered mediators, signaling mechanisms and major signaling crosstalk, Genes Dis. 11 (1) (2023) 103–134.
[16] M. Yu, K. Qin, J. Fan, et al., The Evolving Roles of Wnt Signaling in Stem Cell Proliferation and Differentiation, the Development of Human Diseases, and Therapeutic Opportunities, Genes & Diseases, 2023.
[17] Y. Zhang, D. Wu, X. Zhao, et al., Stem cell-friendly scaffold biomaterials: applications for bone tissue engineering and regenerative medicine, Front. Bioeng. Biotechnol. 8 (2020), 598607.
[18] H. Cheng, W. Jiang, F.M. Phillips, et al., Osteogenic activity of the fourteen types of human bone morphogenetic proteins (BMPs), J. Bone Joint Surg. Am. 85 (8) (2003) 1544–1552.
[19] Q. Kang, W.X. Song, Q. Luo, et al., A comprehensive analysis of the dual roles of BMPs in regulating adipogenic and osteogenic differentiation of mesenchymal progenitor cells, Stem Cell. Dev. 18 (4) (2009) 545–559.
[20] Q. Kang, M.H. Sun, H. Cheng, et al., Characterization of the distinct orthotopic bone-forming activity of 14 BMPs using recombinant adenovirus-mediated gene delivery, Gene Ther. 11 (17) (2004) 1312–1320.
[21] D. Marolt, I.M. Campos, S. Bhumiratana, et al., Engineering bone tissue from human embryonic stem cells, Proc. Natl. Acad. Sci. U. S. A. 109 (22) (2012) 8705–8709.
[22] H. Zhu, T. Kimura, S. Swami, J.Y. Wu, Pluripotent stem cells as a source of osteoblasts for bone tissue regeneration, Biomaterials 196 (2019) 31–45.
[23] D.S. Shenaq, F. Rastegar, D. Petkovic, et al., Mesenchymal progenitor cells and their orthopedic applications: forging a path towards clinical trials, Stem Cell. Int. 2010 (2010), 519028.
[24] E. Huang, Y. Bi, W. Jiang, et al., Conditionally immortalized mouse embryonic fibroblasts retain proliferative activity without compromising multipotent differentiation potential, PLoS One 7 (2) (2012), e32428.
[25] N. Wang, W. Zhang, J. Cui, et al., The piggyBac transposon-mediated expression of SV40 T antigen efficiently immortalizes mouse embryonic fibroblasts (MEFs), PLoS One 9 (5) (2014), e97316.
[26] X. Hu, L. Li, X. Yu, et al., CRISPR/Cas9-mediated reversibly immortalized mouse bone marrow stromal stem cells (BMSCs) retain multipotent features of mesenchymal stem cells (MSCs), Oncotarget 8 (67) (2017) 111847–111865.
[27] D.S. Shenaq, C.M. Teven, I.A. Seitz, et al., Characterization of reversibly immortalized calvarial mesenchymal progenitor cells, J. Craniofac. Surg. 26 (4) (2015) 1207–1213.
[28] S. Lu, J. Wang, J. Ye, et al., Bone morphogenetic protein 9 (BMP9) induces effective bone formation from reversibly immortalized multipotent adipose-derived (iMAD) mesenchymal stem cells, Am. J. Transl. Res. 8 (9) (2016) 3710–3730.
[29] E. Huang, G. Zhu, W. Jiang, et al., Growth hormone synergizes with BMP9 in osteogenic differentiation by activating the JAK/STAT/IGF1 pathway in murine multilineage cells, J. Bone Miner. Res. 27 (7) (2012) 1566–1575.
[30] Y. Gou, Y. Weng, Q. Chen, et al., Carboxymethyl chitosan prolongs adenovirus-mediated expression of IL-10 and ameliorates hepatic fibrosis in a mouse model, Bioeng. Transl. Med. 7 (3) (2022), e10306.
[31] Y. Mao, N. Ni, L. Huang, et al., Argonaute (AGO) proteins play an essential role in mediating BMP9-induced osteogenic signaling in mesenchymal stem cells (MSCs), Genes Dis. 8 (6) (2021) 918–930.
[32] X. Zhao, B. Huang, H. Wang, et al., A functional autophagy pathway is essential for BMP9-induced osteogenic differentiation of mesenchymal stem cells (MSCs), Am. J. Transl. Res. 13 (5) (2021) 4233–4250.
[33] F. He, N. Ni, Z. Zeng, et al., FAMSi: a synthetic biology approach to the fast assembly of multiplex siRNAs for silencing gene expression in mammalian cells, Mol. Ther. Nucleic Acids 22 (2020) 885–899.
[34] B. Zhang, L. Yang, Z. Zeng, et al., Leptin potentiates BMP9-induced osteogenic differentiation of mesenchymal stem cells through the activation of JAK/STAT signaling, Stem Cell. Dev. 29 (8) (2020) 498–510.
[35] N. Wu, H. Zhang, F. Deng, et al., Overexpression of Ad5 precursor terminal protein accelerates recombinant adenovirus packaging and amplification in HEK-293 packaging cells, Gene Ther. 21 (7) (2014) 629–637.
[36] Q. Wei, J. Fan, J. Liao, et al., Engineering the rapid adenovirus production and amplification (RAPA) cell line to expedite the generation of recombinant adenoviruses, Cell. Physiol. Biochem. 41 (6) (2017) 2383–2398.
[37] X. Wu, Z. Li, H. Zhang, et al., Modeling colorectal tumorigenesis using the organoids derived from conditionally immortalized mouse intestinal crypt cells (ciMICs), Genes Dis. 8 (6) (2021) 814–826.
[38] L. Zhang, W. Luo, J. Liu, et al., Modeling lung diseases using reversibly immortalized mouse pulmonary alveolar type 2 cells (imPAC2), Cell Biosci. 12 (1) (2022) 159.
[39] M.R. Rogers, W. Zeng, X. Zhang, et al., Bone Morphogenic Protein 9 (BMP9)/ Growth Differentiation Factor 2 (GDF2) modulates mouse adult hippocampal neurogenesis by regulating the survival of early neural progenitors, Genes Dis. 10 (4) (2023) 1175–1179.
[40] J. Zhong, L. Tian, Y. Gou, et al., BMP4 upregulates glycogen synthesis through the SMAD/SLC2A1 (GLUT1) signaling axis in hepatocellular carcinoma (HCC) cells, Cancer Metabol. 11 (1) (2023) 9.
[41] X. Dong, Y. Gou, M. Guo, et al., A Simplified Noncryogenic Strategy to Transport Mesenchymal Stem Cells: Potential Applications in Cell Therapy and Regenerative Medicine, Genes & Diseases, 2023.
[42] Y. Yu, J. Zhong, C. Chen, et al., SV40 large T antigen-induced immortalization reprograms mouse cardiomyocyte progenitors with mesenchymal stem cell characteristics and osteogenic potential, Genes Dis. 10 (4) (2023) 1161–1164.
[43] R. Li, W. Zhang, Z. Yan, et al., Long non-coding RNA (LncRNA) HOTAIR regulates BMP9-induced osteogenic differentiation by targeting the proliferation of mesenchymal stem cells (MSCs), Aging (Albany NY) 13 (3) (2021) 4199–4214.
[44] L. Huang, J. Zhang, Y. Deng, et al., Niclosamide (NA) overcomes cisplatin resistance in human ovarian cancer, Genes Dis. 10 (4) (2023) 1687–1701.
[45] L. Zhao, L. Huang, J. Zhang, et al., The inhibition of BRAF activity sensitizes chemoresistant human ovarian cancer cells to paclitaxel-induced cytotoxicity and tumor growth inhibition, Am. J. Transl. Res. 12 (12) (2020) 8084–8098.
[46] L. Huang, L. Zhao, J. Zhang, et al., Antiparasitic mebendazole (MBZ) effectively overcomes cisplatin resistance in human ovarian cancer cells by inhibiting multiple cancer-associated signaling pathways, Aging (Albany NY) 13 (13) (2021) 17407–17427.
[47] D. Cao, Y. Lei, Z. Ye, et al., Blockade of IGF/IGF-1R signaling axis with soluble IGF-1R mutants suppresses the cell proliferation and tumor growth of human osteosarcoma, Am. J. Cancer Res. 10 (10) (2020) 3248–3266.
[48] J. Zhong, H. Wang, K. Yang, et al., Reversibly immortalized keratinocytes (iKera) facilitate re-epithelization and skin wound healing: potential applications in cell-based skin tissue engineering, Bioact. Mater. 9 (2022) 523–540.
[49] J. Zhong, Q. Kang, Y. Cao, et al., BMP4 augments the survival of hepatocellular carcinoma (HCC) cells under hypoxia and hypoglycemia conditions by promoting the glycolysis pathway, Am. J. Cancer Res. 11 (3) (2021) 793–811.
[50] X. Yu, F. Liu, L. Zeng, et al., Niclosamide exhibits potent anticancer activity and synergizes with sorafenib in human renal cell cancer cells, Cell. Physiol. Biochem. 47 (3) (2018) 957–971.
[51] J. Fan, Y. Feng, R. Zhang, et al., A simplified system for the effective expression and delivery of functional mature microRNAs in mammalian cells, Cancer Gene Ther. 27 (6) (2020) 424–437.
[52] Q. Zhang, J. Wang, F. Deng, et al., TqPCR: a touchdown qPCR assay with significantly improved detection sensitivity and amplification efficiency of SYBR green qPCR, PLoS One 10 (7) (2015), e0132666.
[53] F. He, N. Ni, H. Wang, et al., OUHP: an optimized universal hairpin primer system for cost-effective and high-throughput RT-qPCR-based quantification of microRNA (miRNA) expression, Nucleic Acids Res. 50 (4) (2022) e22.
[54] H. Wang, Y. Cao, L. Shu, et al., Long non-coding RNA (lncRNA) H19 induces hepatic steatosis through activating MLXIPL and mTORC1 networks in hepatocytes, J. Cell Mol. Med. 24 (2) (2020) 1399–1412.
[55] L. An, Q. Shi, Y. Zhu, et al., Bone morphogenetic protein 4 (BMP4) promotes hepatic glycogen accumulation and reduces glucose level in hepatocytes through mTORC2 signaling pathway, Genes Dis. 8 (4) (2021) 531–544.
[56] M. Guo, Y. Gou, X. Dong, et al., Syrosingopine, an anti-hypertensive drug and lactate transporter (MCT1/4) inhibitor, activates hepatic stellate cells and exacerbates liver fibrosis in a mouse model, Genes & Dis. (2023), 101169.
[57] Y. Zhu, Q. Shi, Q. Peng, et al., A simplified 3D liver microsphere tissue culture model for hepatic cell signaling and drug-induced hepatotoxicity studies, Int. J. Mol. Med. 44 (5) (2019) 1653–1666.
[58] T.C. He, S. Zhou, L.T. da Costa, J. Yu, K.W. Kinzler, B. Vogelstein, A simplified system for generating recombinant adenoviruses, Proc. Natl. Acad. Sci. U. S. A. 95 (5) (1998) 2509–2514.
[59] J. Luo, Z.L. Deng, X. Luo, et al., A protocol for rapid generation of recombinant adenoviruses using the AdEasy system, Nat. Protoc. 2 (5) (2007) 1236–1247.

[60] C.S. Lee, E.S. Bishop, R. Zhang, et al., Adenovirus-mediated gene delivery: potential applications for gene and cell-based therapies in the new era of personalized medicine, Genes Dis. 4 (2) (2017) 43–63.
[61] N. Ni, F. Deng, F. He, et al., A one-step construction of adenovirus (OSCA) system using the Gibson DNA Assembly technology, Mol. Ther. Oncolytics 23 (2021) 602–611.
[62] J. Huang, Y. Bi, G.H. Zhu, et al., Retinoic acid signalling induces the differentiation of mouse fetal liver-derived hepatic progenitor cells, Liver Int. 29 (10) (2009) 1569–1581.
[63] G.H. Zhu, J. Huang, Y. Bi, et al., Activation of RXR and RAR signaling promotes myogenic differentiation of myoblastic C2C12 cells, Differentiation 78 (4) (2009) 195–204.
[64] S. Yan, R. Zhang, K. Wu, et al., Characterization of the essential role of bone morphogenetic protein 9 (BMP9) in osteogenic differentiation of mesenchymal stem cells (MSCs) through RNA interference, Genes Dis. 5 (2) (2018) 172–184.
[65] J. Wang, H. Zhang, W. Zhang, et al., Bone morphogenetic protein-9 effectively induces osteo/odontoblastic differentiation of the reversibly immortalized stem cells of dental apical papilla, Stem Cell. Dev. 23 (12) (2014) 1405–1416.
[66] N. Tang, W.X. Song, J. Luo, et al., BMP-9-induced osteogenic differentiation of mesenchymal progenitors requires functional canonical Wnt/beta-catenin signalling, J. Cell Mol. Med. 13 (8B) (2009) 2448–2464.
[67] D. Song, F. Zhang, R.R. Reid, et al., BMP9 induces osteogenesis and adipogenesis in the immortalized human cranial suture progenitors from the patent sutures of craniosynostosis patients, J. Cell Mol. Med. 21 (11) (2017) 2782–2795.
[68] L.L. Listenberger, A.M. Studer, D.A. Brown, N.E. Wolins, Fluorescent detection of lipid droplets and associated proteins, Curr. Protoc. Cell Biol. 71 (2016) 4.31.31–34.31.14.
[69] J. Cui, W. Zhang, E. Huang, et al., BMP9-induced osteoblastic differentiation requires functional Notch signaling in mesenchymal stem cells, Lab. Invest. 99 (1) (2019) 58–71.
[70] J. Luo, M. Tang, J. Huang, et al., TGFbeta/BMP type I receptors ALK1 and ALK2 are essential for BMP9-induced osteogenic signaling in mesenchymal stem cells, J. Biol. Chem. 285 (38) (2010) 29588–29598.
[71] J. Wang, J. Liao, F. Zhang, et al., NEL-like molecule-1 (Nell1) is regulated by bone morphogenetic protein 9 (BMP9) and potentiates BMP9-induced osteogenic differentiation at the expense of adipogenesis in mesenchymal stem cells, Cell. Physiol. Biochem. 41 (2) (2017) 484–500.
[72] J. Liao, Q. Wei, Y. Zou, et al., Notch signaling augments BMP9-induced bone formation by promoting the osteogenesis-angiogenesis coupling process in mesenchymal stem cells (MSCs), Cell. Physiol. Biochem. 41 (5) (2017) 1905–1923.
[73] J. Liao, X. Yu, X. Hu, et al., lncRNA H19 mediates BMP9-induced osteogenic differentiation of mesenchymal stem cells (MSCs) through Notch signaling, Oncotarget 8 (32) (2017) 53581–53601.
[74] Y. Shu, C. Yang, X. Ji, et al., Reversibly immortalized human umbilical cord-derived mesenchymal stem cells (UC-MSCs) are responsive to BMP9-induced osteogenic and adipogenic differentiation, J. Cell. Biochem. (2018).
[75] X. Liu, J. Qin, Q. Luo, et al., Cross-talk between EGF and BMP9 signalling pathways regulates the osteogenic differentiation of mesenchymal stem cells, J. Cell Mol. Med. 17 (9) (2013) 1160–1172.
[76] Q. Chen, L. Zheng, Y. Zhang, et al., Special AT-rich sequence-binding protein 2 (Satb2) synergizes with Bmp9 and is essential for osteo/odontogenic differentiation of mouse incisor mesenchymal stem cells, Cell Prolif. 54 (4) (2021), e13016.
[77] Z. Yuan, P. Wei, Y. Huang, et al., Injectable PLGA microspheres with tunable magnesium ion release for promoting bone regeneration, Acta Biomater. 85 (2019) 294–309.
[78] Z.P. Dumanian, V. Tollemar, J. Ye, et al., Repair of critical sized cranial defects with BMP9-transduced calvarial cells delivered in a thermoresponsive scaffold, PLoS One 12 (3) (2017), e0172327.
[79] X. Wang, V. Agrawal, C.L. Dunton, et al., Chromatin reprogramming and bone regeneration in vitro and in vivo via the microtopography-induced constriction of cell nuclei, Nat. Biomed. Eng. (2023).
[80] X. Huang, F. Wang, C. Zhao, et al., Dentinogenesis and tooth-alveolar bone complex defects in BMP9/GDF2 knockout mice, Stem Cell. Dev. 28 (10) (2019) 683–694.
[81] Y. Zhang, W. Luo, L. Zheng, et al., Efficient bone regeneration of BMP9-stimulated human periodontal ligament stem cells (hPDLSCs) in decellularized bone matrix (DBM) constructs to model maxillofacial intrabony defect repair, Stem Cell Res. Ther. 13 (1) (2022) 535.
[82] M. Peng, X. Ma, Y. Cao, et al., Comparison of the biomechanical differences in the occlusal movement of wild-type and BMP9 knockout mice with apical periodontitis, Front. Bioeng. Biotechnol. 10 (2022), 1036061.
[83] R. Li, W. Zhang, J. Cui, et al., Targeting BMP9-promoted human osteosarcoma growth by inactivation of notch signaling, Curr. Cancer Drug Targets 14 (3) (2014) 274–285.
[84] Y. Su, X. Luo, B.C. He, et al., Establishment and characterization of a new highly metastatic human osteosarcoma cell line, Clin. Exp. Metastasis 26 (7) (2009) 599–610.
[85] J. Fan, Q. Wei, J. Liao, et al., Noncanonical Wnt signaling plays an important role in modulating canonical Wnt-regulated stemness, proliferation and terminal differentiation of hepatic progenitors, Oncotarget 8 (16) (2017) 27105–27119.
[86] Y. Li, E.R. Wagner, Z. Yan, et al., The calcium-binding protein S100A6 accelerates human osteosarcoma growth by promoting cell proliferation and inhibiting osteogenic differentiation, Cell. Physiol. Biochem. 37 (6) (2015) 2375–2392.
[87] Z. Liao, G. Nan, Z. Yan, et al., The anthelmintic drug niclosamide inhibits the proliferative activity of human osteosarcoma cells by targeting multiple signal pathways, Curr. Cancer Drug Targets 15 (8) (2015) 726–738.
[88] S. Xiao, T. Zhao, J. Wang, et al., Gelatin methacrylate (GelMA)-Based hydrogels for cell transplantation: an effective strategy for tissue engineering, Stem. Cell Rev. Rep. 15 (5) (2019) 664–679.
[89] M. Shen, L. Wang, Y. Gao, et al., 3D bioprinting of in situ vascularized tissue engineered bone for repairing large segmental bone defects, Mater. Today Bio 16 (2022), 100382.
[90] K.A. Sharff, W.X. Song, X. Luo, et al., Hey1 basic helix-loop-helix protein plays an important role in mediating BMP9-induced osteogenic differentiation of mesenchymal progenitor cells, J. Biol. Chem. 284 (1) (2009) 649–659.
[91] Y. Peng, Q. Kang, H. Cheng, et al., Transcriptional characterization of bone morphogenetic proteins (BMPs)-mediated osteogenic signaling, J. Cell. Biochem. 90 (6) (2003) 1149–1165.
[92] Y. Peng, Q. Kang, Q. Luo, et al., Inhibitor of DNA binding/differentiation helix-loop-helix proteins mediate bone morphogenetic protein-induced osteoblast differentiation of mesenchymal stem cells, J. Biol. Chem. 279 (31) (2004) 32941–32949.
[93] L. Zhang, Q. Luo, Y. Shu, et al., Transcriptomic landscape regulated by the 14 types of bone morphogenetic proteins (BMPs) in lineage commitment and differentiation of mesenchymal stem cells (MSCs), Genes Dis. 6 (3) (2019) 258–275.
[94] A.C. Ortiz, S.O.M. Fideles, K.T. Pomini, et al., Effects of therapy with fibrin glue combined with mesenchymal stem cells (MSCs) on bone regeneration: a systematic review, Cells 10 (9) (2021).
[95] D.H. Doro, A.E. Grigoriadis, K.J. Liu, Calvarial suture-derived stem cells and their contribution to cranial bone repair, Front. Physiol. 8 (2017) 956.
[96] H. Zhao, J. Feng, T.V. Ho, W. Grimes, M. Urata, Y. Chai, The suture provides a niche for mesenchymal stem cells of craniofacial bones, Nat. Cell Biol. 17 (4) (2015) 386–396.
[97] F. Jiang, W. Zhang, M. Zhou, et al., Human amniotic mesenchymal stromal cells promote bone regeneration via activating endogenous regeneration, Theranostics 10 (14) (2020) 6216–6230.
[98] L. Xu, Y. Liu, Y. Sun, et al., Tissue source determines the differentiation potentials of mesenchymal stem cells: a comparative study of human mesenchymal stem cells from bone marrow and adipose tissue, Stem Cell Res. Ther. 8 (1) (2017) 275.
[99] W. Zhou, J. Lin, K. Zhao, et al., Single-cell profiles and clinically useful properties of human mesenchymal stem cells of adipose and bone marrow origin, Am. J. Sports Med. 47 (7) (2019) 1722–1733.
[100] Q. Li, H. Yu, M. Sun, et al., The tissue origin effect of extracellular vesicles on cartilage and bone regeneration, Acta Biomater. 125 (2021) 253–266.
[101] I. Harasymiak-Krzyzanowska, A. Niedojadlo, J. Karwat, et al., Adipose tissue-derived stem cells show considerable promise for regenerative medicine applications, Cell. Mol. Biol. Lett. 18 (4) (2013) 479–493.
[102] J.M. Seong, B.C. Kim, J.H. Park, I.K. Kwon, A. Mantalaris, Y.S. Hwang, Stem cells in bone tissue engineering, Biomed. Mater. 5 (6) (2010), 062001.
[103] J. Laloze, L. Fievet, A. Desmouliere, Adipose-derived mesenchymal stromal cells in regenerative medicine: state of play, current clinical trials, and future prospects, Adv. Wound Care 10 (1) (2021) 24–48.
[104] A. Smakaj, D. De Mauro, G. Rovere, et al., Clinical application of adipose derived stem cells for the treatment of aseptic non-unions: current stage and future perspectives-systematic review, Int. J. Mol. Sci. 23 (6) (2022).
[105] K. Czerwiec, M. Zawrzykraj, M. Deptula, et al., Adipose-derived mesenchymal stromal cells in basic research and clinical applications, Int. J. Mol. Sci. 24 (4) (2023).